ACS OMEGA

Open Access

http://pubs.acs.org/journal/acsodf

Article

Tagetes erecta-Mediated Biosynthesis of Mn_3O_4 Nanoparticles: Structural, Electrochemical, and Biological Investigations

Shabbir Hussain,* Ammara Aslam, Affifa Tajammal, Fezah Othman,* Zeeshan Mustafa, Amnah Mohammed Alsuhaibani, Moamen Salaheldeen Refat, Muhammad Shahid, Muhammad Sagir, and Zainul Amiruddin Zakaria*

Cite This: *ACS Omega* 2024, 9, 35408−35419

Read Online

ACCESS | Metrics & More | Article Recommendations

ABSTRACT: Mn_3O_4 nanoparticles (NPs) find diverse applications in the fields of medicine, biomedicine, biosensors, water treatment and purification, electronics, electrochemistry, and photoelectronics. The production of Mn_3O_4 NPs was reported earlier through various physical, chemical, and green routes, but no studies have still been performed on their biosynthesis from *Tagetes erecta*. We synthesized manganese oxide NPs, i.e., $(Mn_3O_4)_L$ and $(Mn_3O_4)_P$ NPs, by utilizing leaves and petals, respectively, of *T. erecta* as reducing and stabilizing agents. The investigated green path is eco-friendly and does not involve any hazardous raw materials. The structural properties of NPs were determined by X-ray diffraction (XRD) analysis, spectroscopies (Fourier transform infrared (FTIR), Raman, and UV−visible), scanning electron microscopy (SEM), thermogravimetric analysis (TGA), and differential scanning calorimetry (DSC). The NPs were also evaluated for their electrochemical properties by cyclic voltammetry (CV) and galvanostatic charge−discharge (GCD). XRD analysis was performed to verify their tetragonal geometry, and the crystallite size (19.24 nm) of $(Mn_3O_4)_P$ was smaller than that (20.84 nm) of $(Mn_3O_4)_L$ NPs. SEM images displayed a porous and spherical morphology with a diameter of 14−35 nm. FTIR spectra of $(Mn_3O_4)_L$ and $(Mn_3O_4)_P$ displayed Mn−O vibrations at 605.69 and 616.87 cm^{-1}, respectively, and the hydrous nature of the material. Raman spectroscopy revealed the existence of tetrahedral and octahedral units along with A_{1g}, T_{2g}, and E_g active modes of Mn_3O_4 and 2TO mode. UV−visible analyses of $(Mn_3O_4)_L$ and $(Mn_3O_4)_P$ NPs showed absorption peaks at 272.3 and 268.8 nm, along with band gaps of 4.83 and 5.49 eV, respectively. TGA curves displayed good thermal stabilities up to 600 °C and a loss of moisture content. DSC curves exhibited exothermic/endothermic peaks with glass transition temperatures of 258.9 and 308.7 °C for $(Mn_3O_4)_P$ and $(Mn_3O_4)_L$, respectively. The CV curves showed redox peaks and confirmed that the electrochemical reaction takes place in the Mn_3O_4 material. GCD scans revealed the capacitive behavior of NPs and their suitability as electrodes in energy storage devices. However, $(Mn_3O_4)_L$ will act as a good material for energy storage applications as compared to $(Mn_3O_4)_P$ NPs. The synthesized NPs were also tested for their antibacterial efficacy by biofilm inhibition and agar well diffusion methods. The NPs showed higher activities against *Staphylococcus aureus* (Gram-positive) than against *Escherichia coli* (Gram-negative), and $(Mn_3O_4)_P$ was more bioactive than $(Mn_3O_4)_L$.

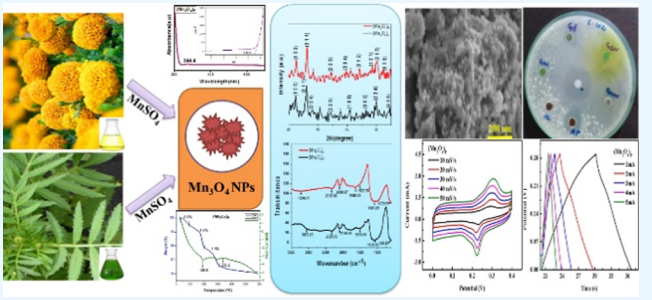

INTRODUCTION

Nanoparticles (NPs) are incredibly interesting as compared to bulk materials of the same chemical compositions because of their high surface-to-volume ratio, small size, and unique physical and chemical properties,[1] which result in their broad-spectrum applications in biological[2] and nonbiological fields.[3] NPs have also been utilized in disease treatment,[2] photocatalysts,[4] battery electrodes,[5] and high-performance supercapacitors.[6] Their role in energy-related applications[7] and the degradation of organic[8] and inorganic contaminants[9] is appreciable.

Manganese, one of the most abundant elements on the planet, has attracted the interest of researchers due to its numerous compositional and structural variants such as MnO_2, Mn_2O_3, MnO, Mn_3O_4, Mn_5O_8, and so on.[10] Mn-based nanomaterials have tremendous potential for long-term nanotechnology. Their unique chemical/physical properties make them ideal for their use in solar cells, molecular sieves, catalysts, batteries, magnetic materials, optoelectronic devices,

Received: February 10, 2024
Revised: May 1, 2024
Accepted: May 16, 2024
Published: August 5, 2024

drug delivery ion sieves, and other fields such as magnetic storage devices, imaging contrast agents, and water purification/treatment.[11] Mn_3O_4 is the most stable oxide of manganese and has been considered the most interesting and important one due to its ferromagnetic properties, high-density magnetic storage medium, high theoretical lithium-storage capacity, and unique ability to remove dyes from aqueous solutions.[12] However, less focus has been paid to manganese as a high-performance metal in some fields including biomedicine, medicine, biosensors, catalysis, photoelectronics, electrochemistry, and electronics. Mn-based nanomaterials exhibit tremendous potential for long-term nanotechnology.[13] The synthesis and characterization of manganese oxides have been in high demand due to their frequent utilization in data storage, pollutant sensing, catalysis, and biological imaging.[14]

Conventional synthetic methodologies for NPs include chemical syntheses, aerosol technologies, UV irradiation, lithography, ultrasonic fields, and photochemical methods, but they involve hazardous substances and high-tech facilities.[15] Moreover, they are expensive, energy-intensive, and time-consuming and require extreme conditions for synthesis. Therefore, alternative green synthetic technologies are required for the elimination of these hazardous effects. In recent years, the synthesis of metal NPs by efficient green chemistry methods has become a key focus of researchers because it offers a superior alternative to traditional procedures.[16] This approach is not only straightforward but also cost-effective, benign, safe, scalable, and operates under ambient conditions. Plant-based biological agents play a dual role as reducing as well as capping agents.[17] Plant-mediated production of NPs is also sustainable for the ecosystem as it is not associated with the menace of toxic waste contamination.[15] Plant-based NPs are significantly more stable than those synthesized by conventional methods, and they are produced in numerous shapes including spherical, needles, cylindrical, cubical, prisms, stems, and dendrites. The nature of the plant extract, metallic salt precursor, and reaction conditions (temperature, pH, and incubation time) greatly affect the properties of generated NPs. Plants are considered as natural "chemical factories," and nature has developed precise and innovative strategies for producing the most valuable nanomaterials.[18]

Plant-mediated green synthesis has been extensively applied in the synthesis of NPs. However, less attention has been given to the green synthesis of Mn_3O_4.[1919] To the best of our knowledge, the synthesis of Mn_3O_4 NPs by utilizing leaf/petal extracts of *Tagetes erecta* has never been reported earlier. The current study was performed to synthesize Mn_3O_4 NPs by using the leaves and petals of *T. erecta*. Structural features of NPs were determined by X-ray diffraction (XRD), scanning electron microscopy (SEM), Fourier transform infrared (FTIR) spectroscopy, Raman spectroscopy, thermogravimetric analysis/differential scanning calorimetry (TGA/DSC), and UV−visible spectroscopy. Their electrochemical properties were investigated by cyclic voltammetry (CV) and galvanostatic charge−discharge (GCD) tests. They were also investigated for their antibacterial potential by agar well diffusion and biofilm inhibition methods.

RESULTS AND DISCUSSION

Aqueous extracts of leaves and petals of *T. erecta* were prepared and mixed with 1 M $MnSO_4 \cdot H_2O$ solution to synthesize the manganese oxide nanoparticles, i.e., $(Mn_3O_4)_L$ and $(Mn_3O_4)_P$, respectively. The synthesized NPs were characterized by various analytical techniques, including XRD, SEM, FTIR spectroscopy, Raman spectroscopy, TGA/DSC, and UV−visible spectroscopy. After structural verification, the electrochemical behavior of the synthesized NPs was tested by an electrochemical workstation. The NPs were also evaluated for their antibacterial efficacy against *Staphylococcus aureus* and *Escherichia coli* (Gram-negative) by two methods (disc diffusion and biofilm inhibition).

Structural Studies by X-ray Diffraction (XRD). The X-ray diffraction technique was used to examine the crystallographic structures of nanoparticles. The synthesized Mn_3O_4 NPs were crystalline, and their diffraction peaks (Figure 1)

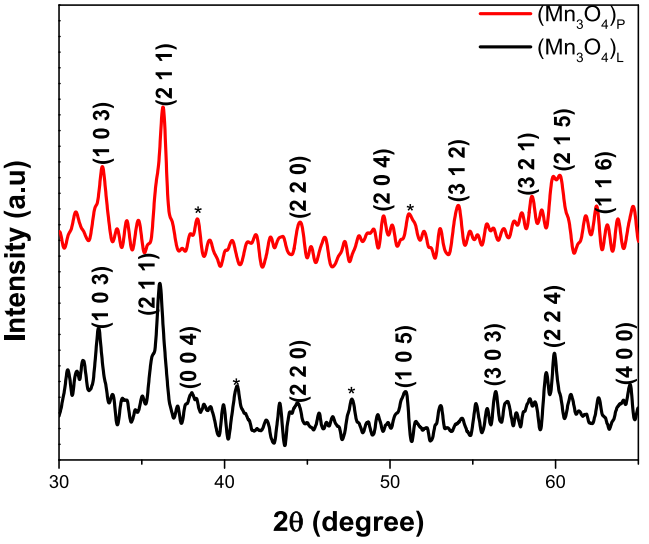

Figure 1. XRD patterns of $(Mn_3O_4)_L$ and $(Mn_3O_4)_P$ NPs.

were in agreement with the standard JCPDS card #24-0734. The Debye−Scherrer equation (eq 1) was used to calculate the crystallite sizes of the NPs.

$$D = \frac{K\lambda}{\beta \cos \theta} \quad (1)$$

where D indicates the crystallite size of the particles, K represents the Scherrer constant (equal to 0.9), λ is the wavelength of light used for diffraction (λ = 1.54 Å), β is the full width at half-maximum (fwhm) of the diffraction peak, and θ is the angle of deflection.

The XRD graph of $(Mn_3O_4)_L$ showed three prominent peaks at 2θ = 33.5, 36.2, and 59.9°, which correspond to the (103), (211), and (224) crystal planes, respectively. However, many small peaks were also observed. In the case of $(Mn_3O_4)_P$, prominent XRD peaks were observed at 2θ = 33.5, 36.2, and 59.5°, which are associated with the (103), (211), and (215) crystal planes, respectively. In both XRD patterns, the (103) and (211) planes were observed. The average crystallite sizes of $(Mn_3O_4)_L$ and $(Mn_3O_4)_P$ calculated by the Debye−Scherrer equation were found to be 20.84 and 19.24 nm, respectively. The XRD results support the tetragonal body-centered lattice structure of Mn_3O_4 NPs.[20] The peak marked with an asterisk in the graph (Figure 1) indicates the presence of water or some contaminations from the plant source.

FTIR Spectroscopy. FTIR spectroscopy of the synthesized NPs was performed in the range of 4000−600 cm^{-1}. The obtained FTIR spectra are shown in Figure 2. The Mn−O

https://doi.org/10.1021/acsomega.4c01328
ACS Omega 2024, 9, 35408−35419

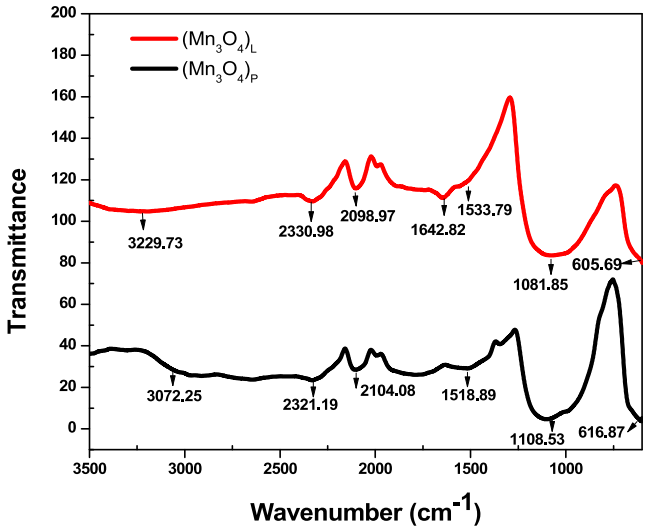

Figure 2. FTIR spectra of $(Mn_3O_4)_L$ and $(Mn_3O_4)_P$ NPs.

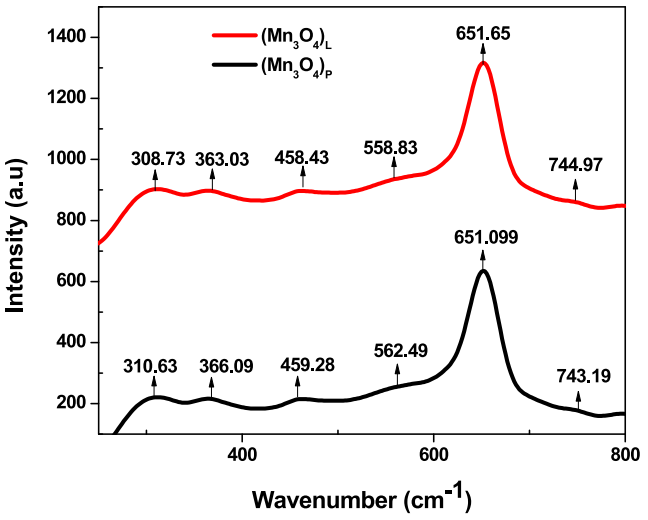

Figure 3. Raman spectra of $(Mn_3O_4)_L$ and $(Mn_3O_4)_P$ NPs.

stretching modes appear as sharp peaks at 605.69 and 616.87 cm^{-1} in $(Mn_3O_4)_L$ and $(Mn_3O_4)_P$, respectively, and represent A_{1g} mode of Mn^{2+} ions at tetrahedral sites.[21] Moreover, smaller bands at 2330.98 and 2321.19 cm^{-1} in (Mn_3O_4) and $(Mn_3O_4)_P$, respectively, were observed, which were attributed to the coupling of the scissor bending and a broad liberation band in the near-infrared region. Absorption bands at 2098.97 and 2104.08 cm^{-1} in (Mn_3O_4) and $(Mn_3O_4)_P$, respectively, represent the existence of hydrogen bonding within the sample.[22] A high-frequency band at 1081.85 cm^{-1} in $(Mn_3O_4)_L$ and 1108.53 cm^{-1} in $(Mn_3O_4)_P$ may be attributed to the υ(Mn−O−H) vibration;[23] this band has a complex origin and envelops two bands related to the TO + LO and 2LO modes in the MnO phase of Mn_3O_4.[24]

The two broad bands at 3229.73 and 1543.11 cm^{-1} in $(Mn_3O_4)_L$ and at 3072.25 and 1518.85 cm^{-1} in $(Mn_3O_4)_P$ represent the stretching and bending vibrations, respectively, of water.[25] The vibrational band at 1642.82 cm^{-1} displays the H−O−H scissor bending[26] and the presence of adsorbed water molecules.[27] All of these vibrations clarify the adsorption of water by the Mn_3O_4 material from atmospheric moisture.[28] The hydrous nature of Mn_3O_4 NPs is also supported by the literature.[12] The hydrated properties of Mn_3O_4 NPs may increase the cation diffusion, thus improving the capacitance of materials.[22] The existence of moisture in the synthesized NPs was also further verified from the thermogravimetric data (discussed in the relevant section).

Raman Spectroscopy. Figure 3 displays the Raman spectra of the synthesized Mn_3O_4 NPs. The literature[29,30] reports that all of the manganese oxides display a strong phonon band at 640−660 cm^{-1} and weak phonon bands in the Raman region of 200−480 cm^{-1}; the Mn_3O_4 NPs investigated by us also displayed the same Raman scattering pattern (Figure 3). Three strong peaks at 651.65, 363.03, and 308.73 cm^{-1} in $(Mn_3O_4)_L$ and at 651.099, 366.09, and 310.63 cm^{-1} in $(Mn_3O_4)_P$ are characteristic of A_{1g}, T_{2g}, and E_g active modes of Mn_3O_4, respectively.[31,32] A strong peak around 651 cm^{-1} demonstrates the presence of hausmannite with a spinel structure, corresponding to the Mn−O stretching vibrations of divalent manganese ions in the tetrahedral coordination.[31]

The simultaneous existence of a phonon band with a large scattering intensity around 651.65 cm^{-1} and a weak band at 743−745 cm^{-1} indicates A_{1g} spectroscopic species with symmetric vibrations of ν_2(Mn−O) and ν_1(Mn−O), respectively.[29,33] Furthermore, the presence of a weak phonon band at 458.43−459.28 cm^{-1} demonstrates the ν_5(Mn−O) symmetric vibration,[30] whereas two weak bands at 308.73 and 363.03 cm^{-1} in $(Mn_3O_4)_L$ and at 310.63 and 366.09 cm^{-1} in $(Mn_3O_4)_P$ are characteristic of Mn−O bending vibrations.[29,30] Most of the vibrations found in these spectra were related to the motion of the oxygen atoms within the MnO_6 octahedral units in Mn_3O_4.[29,30] Weak intensity bands at 558.83 and 562.49 cm^{-1} in $(Mn_3O_4)_L$ and $(Mn_3O_4)_L$, respectively, were assigned to Mn−O−Mn bending vibrations[31] and are indicative of 2TO (transverse optical) mode.[24]

UV−Visible Spectroscopy. The NPs were subjected to UV−visible spectroscopy in the 200−800 nm range; the obtained spectra are shown in Figure 4. The $(Mn_3O_4)_L$ and $(Mn_3O_4)_P$ NPs displayed absorption maxima at 272.3 and 268.8 nm, respectively, which represent $O^{2-} \rightarrow Mn^{2+}$ charge-transfer transitions.[12] The $(Mn_3O_4)_L$ NPs showed smaller band gaps (4.83 eV) than those (5.49 eV) of $(Mn_3O_4)_P$ (Figure 4).

Scanning Electron Microscopy (SEM). Scanned electron microscopy (SEM) was performed to examine the morphology and sizes of the synthesized NPs. Figure 5 shows the SEM images of the $(Mn_3O_4)_L$ and $(Mn_3O_4)_P$ NPs. SEM analysis revealed that the basic surface structures of Mn_3O_4 NPs were porous and spherical, and they have a tendency to agglomerate in some portions.[34] Agglomeration occurs due to the adhesion of NPs to each other by weak forces, leading to (sub)-micronized entities. The NP aggregates are produced due to the formation of metallic or covalent bonds that cannot be disrupted easily.[35] However, SEM findings of Mn_3O_4 nanoparticles agreed with the XRD data. The particle sizes (diameters) of $(Mn_3O_4)_L$ and $(Mn_3O_4)_P$ were found to be approximately 14−35 nm, with larger sizes compared to the latter.

Thermogravimetric Analysis (TGA) and Differential Scanning Calorimetry (DSC). The thermal stabilities and weight loss percentages of NPs were investigated by subjecting them to thermogravimetric analysis (TGA) in the range of 0−600 °C (Figures 6 and 7). The total weight losses of $(Mn_3O_4)_L$ and $(Mn_3O_4)_P$ were found to be only 9.6 and 3.75%, respectively, up to the temperature of 600 °C, indicating their good thermal stabilities and heat resistance; $(Mn_3O_4)_P$

https://doi.org/10.1021/acsomega.4c01328
ACS Omega 2024, 9, 35408−35419

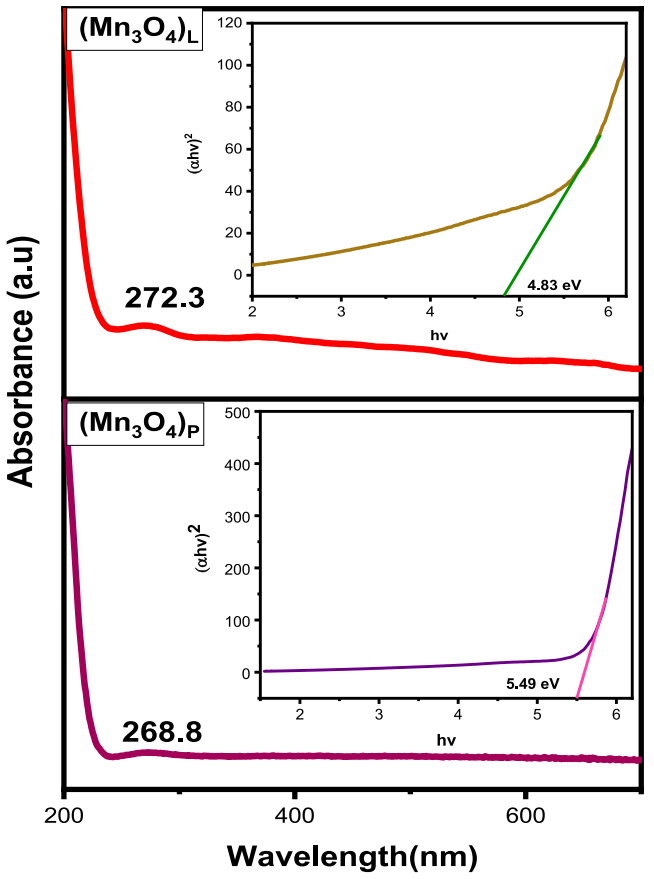

Figure 4. UV−visible spectra of $(Mn_3O_4)_L$ and $(Mn_3O_4)_P$ NPs.

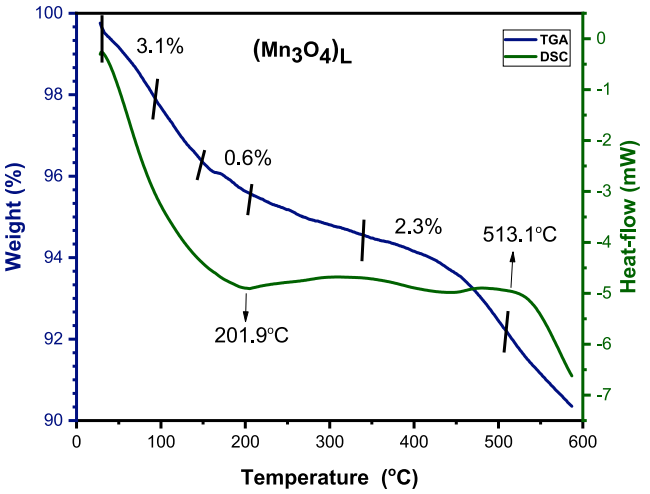

Figure 6. TGA−DSC of $(Mn_3O_4)_L$.

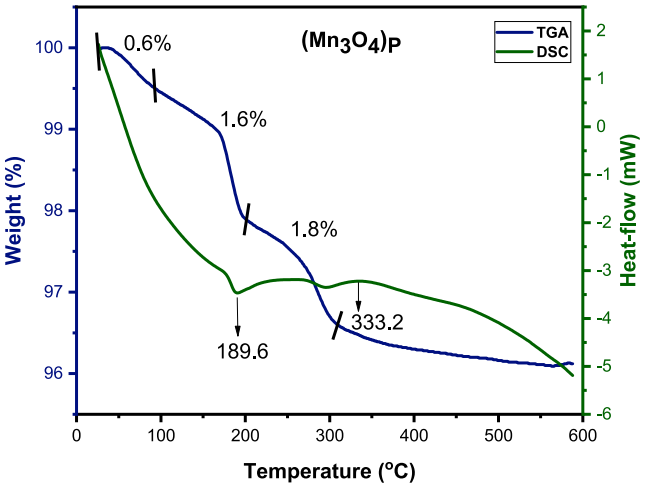

Figure 7. TGA−DSC of $(Mn_3O_4)_P$.

was more thermally stable and resistant to heat as compared to $(Mn_3O_4)_L$. In $(Mn_3O_4)_P$, a gradual loss of weight was observed up to the temperature of 600 °C corresponding to the elimination of adsorbed/coordinated water. The TGA graphs (Figures 6 and 7) revealed a three-stage decomposition pattern of $(Mn_3O_4)_P$. The initial weight loss in $(Mn_3O_4)_P$ at 25−92 °C was attributed to moisture evaporation, whereas the second and third weight loss steps at 114.6−202.7 and 202−310 °C, respectively, were attributed to the loss of adsorbed/coordinated water molecules. These findings are further verified from FTIR data, which demonstrate the existence of water molecules in the lattice of NPs.

The differential scanning calorimetry (DSC) curves (Figures 6 and 7) displayed endothermic peaks in $(Mn_3O_4)_L$ and $(Mn_3O_4)_P$ at 201.9 and 189.6 °C, respectively. Exothermic peaks of $(Mn_3O_4)_L$ and $(Mn_3O_4)_P$ appeared at 513.1 and 333.2 °C, respectively. The glass transition temperatures (at the midpoint of half height) were measured using Moynihan's approach and were found to be 308.7 and 258.9 °C for $(Mn_3O_4)_L$ and $(Mn_3O_4)_P$, respectively.

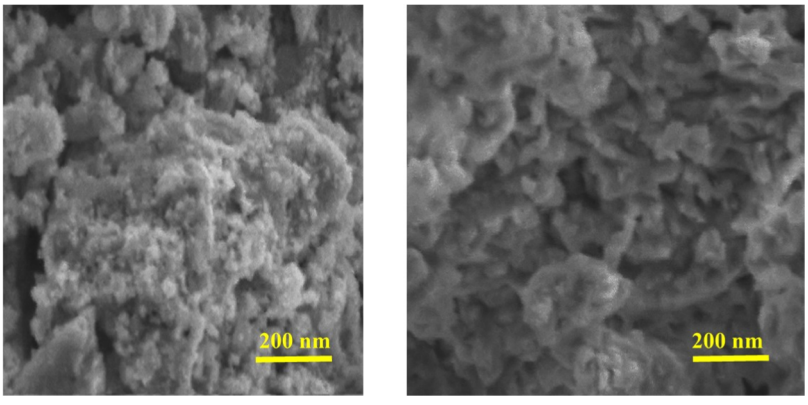

Figure 5. SEM images of $(Mn_3O_4)_L$ (left) and $(Mn_3O_4)_P$ (right) NPs.

https://doi.org/10.1021/acsomega.4c01328
ACS Omega 2024, 9, 35408−35419

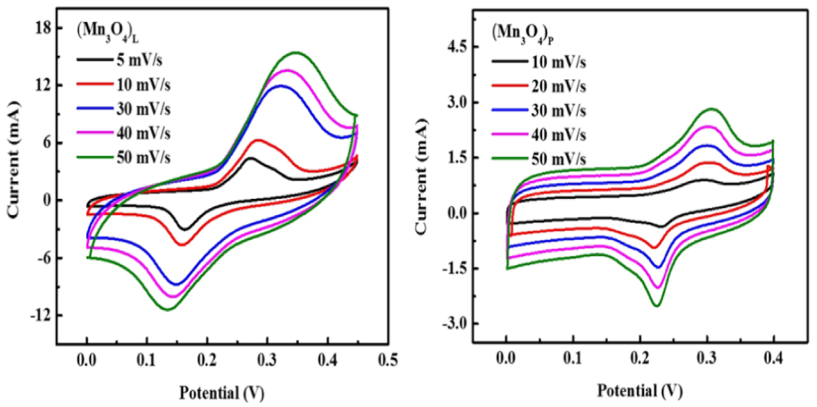

Figure 8. CV curves of $(Mn_3O_4)_L$ (left) and $(Mn_3O_4)_P$ (right) at different scan rates.

Table 1. Calculation of the Redox Current and Redox Potential of $(Mn_3O_4)_L$

scan rate (mV s^{-1})	anodic potential, V_a (V)	cathodic potential, V_c (V)	total redox potential (V)	anodic current, I_a (mA)	cathodic current, I_c (mA)	total redox current (mA)
5	0.271	0.166	0.105	4.5	−2.9	1.6
10	0.283	0.159	0.124	6.3	−4.6	1.7
30	0.320	0.148	0.172	11.8	−8.7	3.1
40	0.330	0.142	0.188	13.6	−10.7	2.9
50	0.335	0.138	0.197	15.4	−11.4	4

Table 2. Calculation of the Redox Current and Redox Potential of $(Mn_3O_4)_P$

scan rate (mV s^{-1})	anodic potential, V_a (V)	cathodic potential, V_c (V)	total redox potential (V)	anodic current, I_a (mA)	cathodic current, I_c (mA)	total redox current (mA)
10	0.290	0.231	0.059	0.906	−0.378	0.528
20	0.294	0.229	0.064	1.390	−0.926	0.464
30	0.296	0.226	0.070	1.840	−1.445	0.395
40	0.299	0.227	0.072	2.359	−1.973	0.386
50	0.303	0.225	0.077	2.843	−2.499	0.344

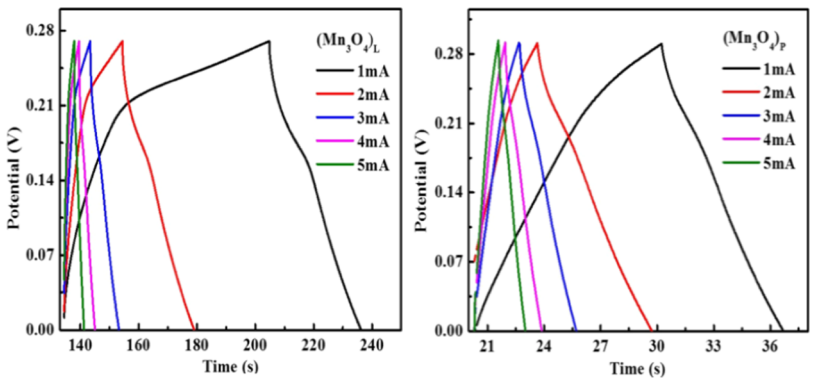

Figure 9. GCD curves of $(Mn_3O_4)_L$ (left) and $(Mn_3O_4)_P$ (right).

Electrochemical Studies. *Cyclic Voltammetry (CV).* Cyclic voltammetry (CV) studies were performed by using an electrochemical workstation within a potential range of 0−0.45 V at different scan rates. Figure 8 displays the CV graphs of $(Mn_3O_4)_L$ and $(Mn_3O_4)_P$ NPs, respectively, whereas the obtained data are summarized in Tables 1 and 2, respectively. At scan rates of 10, 30, 40, and 50 mV s^{-1}, the values of redox potentials of $(Mn_3O_4)_L$ were observed to be 0.124, 0.172, 0.188, and 0.197 V with current values of 0.011, 0.128, 0.023, and 0.003 mA, respectively. At the same scan rates (10−50 mV s^{-1}), the values of redox potentials of $(Mn_3O_4)_P$ NPs were found to be 0.0591, 0.0649, 0.0702, 0.0724, and 0.0774 V with current values 12.34, 8.953, 0.0193, 0.025, and 0.0053A, respectively.[36]

The oxidation−reduction peaks of the NPs were clearly visible on the cyclic voltammograms of synthesized NPs, confirming that both materials were electrochemically active. It was found from the CV curves that the reduction peak potential fluctuates more between 0.2 and 0.3 V. For both samples of $(Mn_3O_4)_L$ and $(Mn_3O_4)_P$, the oxidation peaks of NPs demonstrated a significant area under their corresponding curves, indicating a large value of specific capacitance. The CV curves (Figure 8) of both samples clearly display the redox peaks, demonstrating that the charging process is reversible in

https://doi.org/10.1021/acsomega.4c01328
ACS Omega 2024, 9, 35408−35419

the synthesized Mn_3O_4 materials. The values of the GCD potential were set by observing the CV curves.

Galvanostatic Charge–Discharge. Galvanostatic charge–discharge (GCD) tests of $(Mn_3O_4)_L$ and $(Mn_3O_4)_P$ NPs were performed in a potential range of 0–0.27 V at various current densities. A 6 M KOH solution was used as the electrolyte. The obtained charge–discharge curves were used for the calculation of specific capacitance (C_m) via eq 2.

$$C_m = \frac{C}{m} = \frac{I \times \Delta t}{\Delta V \times m} \quad (2)$$

Here I is the applied current (A), V is the potential window (V), m is the mass of the active material (g), and t is the time of a discharge cycle. All of the electrochemical experiments were performed at a constant temperature.

The GCD curves of $(Mn_3O_4)_L$ and $(Mn_3O_4)_P$ electrode materials are displayed in Figure 9 at different current densities. The observed values of charge/discharge time and the corresponding specific capacitances are given in Tables 3 and 4. The observed peaks were not linear in nature, which confirms that the electrochemical reactions take place while charging and discharging. The maximum charge and discharge capacitances (at a low current density) were observed to be 133.92 and 89.76 mAh g^{-1}, respectively, in $(Mn_3O_4)_L$ and 34.86 and 28.56 mAh g^{-1}, respectively, in $(Mn_3O_4)_P$.

Table 3. Calculated Results of the GCD Curve of $(Mn_3O_4)_L$ NPs

	time (h)		specific capacitance (mAh g^{-1})	
current density (mA)	Δt (charge)	Δt (discharge)	charge capacitance	discharge capacitance
1	1.1697	0.523	133.92	89.76
2	0.33	0.267	76.58	57.034
3	0.147	0.164	55.24	53.85
4	0.072	0.088	48.16	38.49
5	0.0572	0.0571	37.81	31.45

Table 4. Calculated Results of the GCD Curve of $(Mn_3O_4)_P$ NPs

	time (h)		specific capacitances (mAh g^{-1})	
current density (mA)	Δt (charge)	Δt (discharge)	charge capacitance	discharge capacitance
1	0.162	0.107	34.86	28.56
2	0.0546	0.107	24.82	22.09
3	0.038	0.12	22.15	20.48
4	0.025	0.032	20.33	18.49
5	0.621	0.0234	17.62	16.203

The GCD curves of $(Mn_3O_4)_P$ clearly show a linear behavior compared to those of $(Mn_3O_4)_L$ NPs. The charge/discharge cycle time of $(Mn_3O_4)_P$ NPs was less than that of $(Mn_3O_4)_L$ NPs. Although the material charging of $(Mn_3O_4)_P$ NPs was fast, the calculated capacitance of $(Mn_3O_4)_P$ NPs was less than that of $(Mn_3O_4)_L$ NPs.

Antibacterial Activity. $(Mn_3O_4)_L$ and $(Mn_3O_4)_P$ were tested for their antibacterial potential against *E. coli* (Gram-negative) and *S. aureus* (Gram-positive) by the biofilm inhibition[37] and agar well diffusion[38] methods, whereas ciprofloxacin was applied as the standard reference drug. Ciprofloxacin was used as the positive control, while water was employed as the negative control. The obtained data are displayed in Table 5, whereas inhibition zones (formed around wells) are shown in Figure 10.

Table 5. Antibacterial Activity Data of the Synthesized NPs

	biofilm inhibition (%)		inhibition zones (mm)	
sample	*E. coli*	*S. aureus*	*E. coli*	*S. aureus*
$(Mn_3O_4)_L$	0	0	3	12
$(Mn_3O_4)_P$	3	0	15	21
ciprofloxacin	53	47	40	37

$(Mn_3O_4)_L$ did not exhibit any biofilm inhibition of either *E. coli* or *S. aureus*; however, $(Mn_3O_4)_P$ was found to be slightly active against *E. coli* with a biofilm inhibition of 3% as compared to that of ciprofloxacin (53%). Promising antibacterial potentials were exhibited by $(Mn_3O_4)_L$ and $(Mn_3O_4)_P$ in the agar well diffusion method; both NP samples showed comparatively large inhibition zones against *S. aureus* as compared to those against *E. coli* (Table 5). The higher activity against *S. aureus* can be attributed to the structural differences between the cell walls of G-negative (*E. coli*) and G-positive (*S. aureus*) bacteria. In G-negative bacteria, the thin peptidoglycan layer is enveloped by an outer membrane; there is also the presence of periplasm between the plasma membrane and the outer layer. This periplasm is a part of neither the protoplast (because it lies above the plasma membrane) nor the external environment (because it is covered by an outer membrane).[39,40] Consequently, the cell wall of G-negative bacteria is able to protect the contents of the cell due to its remarkable toughness, elasticity, and strength as compared to G-positive bacteria.[39] As the cell walls of G-positive bacteria have no outer lipid membranes,[41] they are considered to be relatively simple structural entities.[39]

The agar well diffusion data (Table 5) evidently depict the higher antibacterial efficacy (large inhibition zones) of $(Mn_3O_4)_P$ NPs compared to that of $(Mn_3O_4)_L$ (small inhibition zones). The differences in activities of both kinds of manganese oxide NPs may be attributed to the differences in the particle sizes of NPs. However, the phytochemical composition of plant coatings upon the surfaces of NPs may also play an important role in the biological potential as the surfaces of $(Mn_3O_4)_L$ and $(Mn_3O_4)_P$ NPs were coated by leaves and petal extracts, respectively, of *T. erecta*. These findings thus clarify the role of plant materials in defining the biological potential of the biosynthesized nanomaterials and elaborate the presence of more bioactive ingredients in the petal extracts as compared to the corresponding leaf extract of the same plant (*T. erecta*). Earlier reports[42] also recommend the use of *T. erecta* flowers (petals) as an alternative source of antimicrobial agents against human pathogens. It is worth mentioning that both of the synthesized NPs showed lower activities as compared to ciprofloxacin (reference drug).

Comparison of the Investigated Work with Previous Studies. We synthesized $(Mn_3O_4)_L$ and $(Mn_3O_4)_P$ from manganese sulfate precursors by employing the eco-friendly and abundantly available solvent, i.e., water. The investigated route is very simple and does not involve any toxic agents. It utilizes aqueous extracts of *T. erecta* as reducing and stabilizing agents. *T. erecta* is an easily available wild herb worldwide and is also cultivated in various parts of the world. The synthesized NPs had crystallite sizes of 19.24–20.84 nm with a tetragonal

https://doi.org/10.1021/acsomega.4c01328
ACS Omega 2024, 9, 35408–35419

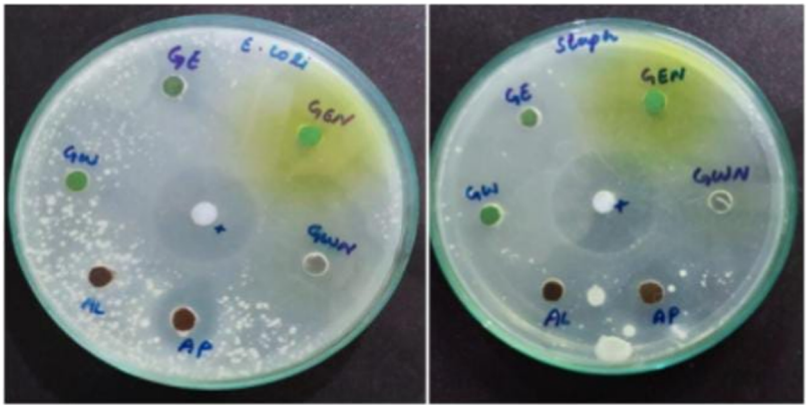

Figure 10. Inhibition zones (mm) of $(Mn_3O_4)_L$ = AL and $(Mn_3O_4)_P$ = AP against *E. coli* (left) and *S. aureus* (right) measured by a vernier caliper by the agar well diffusion method.

Table 6. Comparison of Important Properties and Applications of Earlier Reported Mn_3O_4 NPs

sl. no.	extract of plant used	precursor metal salt	particle sizes and shapes	applications performed	refs
1	*Taxus baccata* acetone extract	$KMnO_4$	32 nm size, spherical with tetragonal spinel structures	cytotoxicity against murine macrophage cell line J774-A1 and U87 glioblastoma cancer cells; for mortality in *Leishmania major*	43
2	aqueous extract of *Helianthus annuus* seed cake	manganese acetate	spherical with size in the range of 10−70 nm	effect on biological growth of *Vigna radiata*	44
3	aqueous extract of *Phoenix dactylifera* (date pits)		14.1 nm and agglomerated (annealed at 500 °C); 23.6 nm polyhedron and tetrahedron (annealed at 700 °C)	electrochemical analysis	12
4	aqueous extract of *Aspalathus linearis*	$MnCl_2{\cdot}4H_2O$	17−28 nm, quasi-spherical, tetragonally distorted cubic lattices	photoluminescence; for emission devices	19
5	*Simarouba glauca* leaf extract	manganese(II) acetate	15 nm size; tetragonal crystalline with spherical morphology	photocatalytic degradation of malachite green dye	45
6	chia seeds extract	$MnCl_2{\cdot}4H_2O$	35.27 nm	cytotoxicity on the HL-60 cells; safety as a drug	46
7	aqueous extract of *Dalbergiella welwitschia* leaves	$MnCl_2{\cdot}4H_2O$	37.149 nm size; body-centered tetragonal	α-glucosidase enzyme inhibition and anti-inflammatory studies	47
8	*Prunus dulcis* (almond) leaves, seed, and seed oil	manganese sulfate	44−99, 84−126, and 49−160 nm prepared from almond leaves, seeds, and seed oil, respectively; quasi-spherical	bactericidal; antioxidant; in vitro cytotoxicity	48
9	*Pistacia lentiscus* leaves	$Mn(NO_3)_2{\cdot}4H_2O$	37 nm; spherical	photocatalyst for dye pollutant degradation	49
10	green tea extract	$KMnO_4$	olive-shaped with some cubic particles	catalytic oxidation (degradation) of estriol (E3); catalyst for activation of peroxydisulfate	50
11	aqueous extract of *Azadirachta indica* (Neem) leaves	manganese(II) acetate tetrahydrate		catalytic thermal decomposition of ammonium perchlorate; as a working electrode for fabricating chemical sensors	28
12	*Costus woodsonii* flowers	$MnCl_2{\cdot}4H_2O$		potential adsorbent for the removal of malachite green dye from water	51

body-centered lattice and possessed good thermal stabilities. They showed significant antimicrobial potential by the agar well diffusion method and also little biofilm inhibition of G-negative (*E. coli*) and G-positive (*S. aureus*) bacteria. Electrochemical studies have reported their prominent redox peaks with a reversible charging−discharging behavior; moreover, they were found to be suitable as an electrode material for supercapacitors.

Earlier studies (Table 6) investigated the plant-mediated synthesis of Mn_3O_4 NPs by employing various metal salt precursors including potassium permanganate, manganese(II) acetate, manganese(II) chloride tetrahydrate, manganese sulfate monohydrate, and manganese(II) nitrate tetrahydrate, and they reported various sizes (10−70 nm) of NPs with different morphologies, e.g., spherical, spherical with tetragonal spinel structures, agglomerated, scaly and cubic shapes, quasi-spherical, tetragonally distorted cubic lattices, and olive shapes with small cubic particles. Such studies also reported numerous applications of Mn_3O_4 NPs, which include cytotoxicity, biological growth, photoluminescence, photocatalytic degradation of dyes, α-glucosidase enzyme inhibition, anti-inflammatory studies, antioxidant, bactericidal, catalytic oxidation, catalytic thermal decomposition, and as a working electrode for fabricating chemical sensors. However, electrochemical investigations of plant-synthesized Mn_3O_4 NPs have been rarely reported earlier (Table 6).

EXPERIMENTAL SECTION

Materials and Methods. Manganese sulfate monohydrate (≥99%) was purchased from Sigma-Aldrich. Distilled water was used as the solvent for the synthesis of NPs. Nutrient agar and nutrient broth were procured from Oxiod, U.K. Structural analyses of Mn_3O_4 NPs were performed by using an advanced X-ray diffractometer (XRD) of model Bruker AXS, D8. FTIR spectroscopy was performed by a Carry 630 Fourier transform Infra-Red spectrometer. Raman spectra were recorded by a

https://doi.org/10.1021/acsomega.4c01328
ACS Omega 2024, 9, 35408−35419

Figure 11. Leaves (left) and flowers (right) of *T. erecta*.

Figure 12. Leaf (left) and flower (right) powders of *T. erecta*.

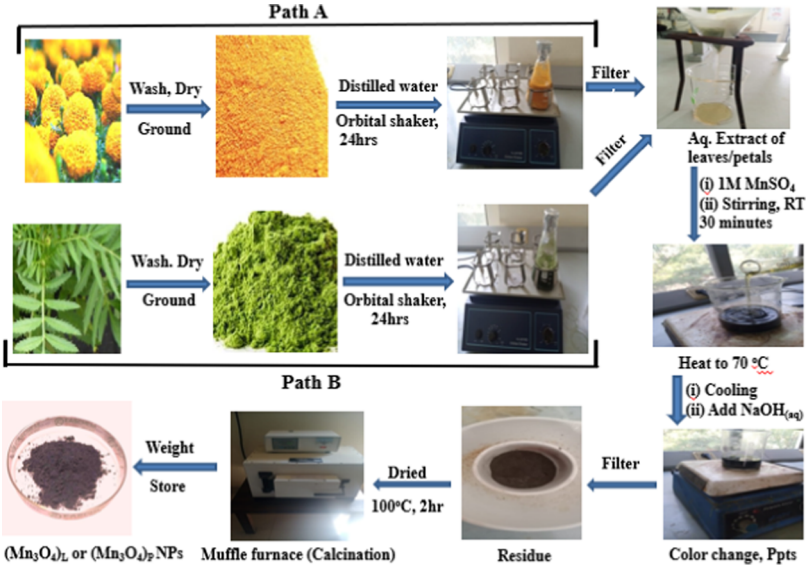

Figure 13. Biosynthetic route of $(Mn_3O_4)_L$ and $(Mn_3O_4)_L$ NPs using the aqueous extracts of leaves and petals, respectively, of *T. erecta*.

Renishaw Vis Reflex Raman spectrometer. UV−visible spectroscopic analysis was performed by a SPECORD 200 PLUS spectrometer. SEM analysis was performed by a Hitachi S4800. The synthesized NPs were subjected to differential scanning calorimetry (DSC) and thermogravimetric analysis by an SDT (Q600) thermal analyzer (TA Instruments) under a nitrogen atmosphere at a heating rate of 20 °C min^{-1}. A galvanostat/potentiostat of model CS-300, China, was used to determine the electrochemical properties and charging/discharging potentials of the nanoparticles by a reported procedure.[52]

Antibacterial activities of the synthesized NPs were determined against *S. aureus* (Gram-positive) and *E. coli* (Gram-negative) by using reported procedures of biofilm inhibition[37] and agar well diffusion[38] methods, whereas ciprofloxacin was applied as the standard reference drug. The Institute of Microbiology at the University of Agriculture Faisalabad, Pakistan, verified the identities and purities of the bacterial strains. The antibacterial activities were performed at the Department of Biochemistry, University of Agriculture Faisalabad, Pakistan. Nutrient agar was used as the growth medium for the bacteria. A vernier caliper was used to measure the diameters of the inhibition zones (around wells) in

https://doi.org/10.1021/acsomega.4c01328
ACS Omega 2024, 9, 35408−35419

millimeters,[38] whereas a microplate reader (BioTek) was used to measure the optical density (OD) of each well at 630 nm.[37]

Identification and Collection of Plant Materials. Leaves and petals of *T. erecta* plants (Figure 11) were collected from the fields of Pattoki (Punjab), Pakistan, in November 2021. The plant material was identified by the Department of Biology, Lahore Garrison University, Lahore, Pakistan. The collected samples (leaves and petals) were washed with distilled water many times for the removal of dust particles, dried in the shade for 2 weeks, and then ground with the help of a grinder until they turned into a fine powder (Figure 12). The fine powders of leaves and petals were sieved separately with an 80 mesh size and then stored in polythene bags at room temperature for further use.

Preparation of Aqueous Extracts of *T. erecta* Leaves and Petals. 100 g of dried powder of leaf/petals of *T. erecta* plants was mixed with 500 mL of distilled water, kept in an orbital shaker for 24 h at room temperature, and then filtered through Whatman No. 1 filter paper. Green- and yellow-colored extracts of the leaves and petals, respectively, were obtained, which were stored at 4 °C until further use (Figure 13). Paths A and B in Figure 13 display the preparation of aqueous extracts of leaves and petals, respectively, of *T. erecta*.

Preparation of $(Mn_3O_4)_L$ and $(Mn_3O_4)_P$ NPs. Twenty milliliters of freshly prepared manganese sulfate solution (1 M) was stirred with 20 mL of aqueous extract of *T. erecta* leaves at room temperature. After 30 min, the temperature was increased to 70 °C. There was no change in the color of the solution. The flask was kept aside to cool down to room temperature. After cooling, the flask was again placed on a magnetic stirrer, and 20 mL of 1 M NaOH solution was added dropwise with the help of a dropper. There was a sudden change in the color along with the formation of precipitates in the reaction mixture, which clearly indicated the formation of NPs. The precipitates were separated by filtration through Whatman filter paper No. 1 and rinsed with distilled water. They were dried in an oven at 100 °C for 2 h, then ground into a fine dark-brown powder, which was taken in a China dish, and finally placed in a muffle furnace for 2 h at 500 °C. The final product of $(Mn_3O_4)_L$ NPs (1.48 g) was stored for analysis and further use. The same procedure was applied for the synthesis of $(Mn_3O_4)_P$ NPs (1.68 g) by using the petal powder of *T. erecta* at room temperature in place of the leaf powder of the same plant. The whole biosynthetic pathway for the formation of $(Mn_3O_4)_L$ and $(Mn_3O_4)_L$ NPs using the aqueous extracts of leaves and petals, respectively, of *T. erecta* is summarized in Figure 13.

Cyclic Voltammetry (CV) and Galvanostatic Charge–Discharge (GCD) Test. The synthesized Mn_3O_4 NPs were evaluated for their electrochemical potential by cyclic voltammetry and galvanostatic charge–discharge (GCD) tests by a reported procedure. Cyclic voltammetry (CV) was carried out using a CS-300 electrochemical workstation. In a three-electrode cell configuration, a platinum wire and Ag/AgCl were used as the counter and reference electrodes, respectively. The loading density of the electroactive materials was 0.1 mg cm^{-2}. A 6 M KOH aqueous solution was used as the electrolyte due to its good conductivity. The solution of this concentration offers an excellent concentration of OH^- ions as compared to the other concentrations, thus facilitating charge transfer in bulk electrodes.

The working electrode was prepared by taking a small piece of nickel foam and washing it with ethanol and deionized water (DI) followed by sonication for 10 min. Then, the nickel foam was dried using a dryer. A mixture of 80% NPs (leaves/petals), 15% carbon charcoal, and 5% binder was ground with a mortar and pestle to obtain a fine powder. A few drops of *N*-methyl-2-pyrrolidone (NMP) were also added to form a slurry. Nickel foam was dipped into the slurry and then dried at 70 °C overnight.[52]

Determination of the Antibacterial Potential by a Biofilm Inhibition Assay (Microtiter Plate Method). The synthesized NPs were tested for their antibiofilm potential by a reported microtiter plate technique[37] using ciprofloxacin as a reference drug. Each well of a sterile 96-well plastic tissue culture plate (having a flat bottom) was filled with 20 μL of a bacterial suspension (*S. aureus* or *E. coli*), 100 μL of the testing solution, and 100 μL of nutrient broth. As the negative control, wells containing only the nutrient broth were used. Each plate was covered and incubated aerobically for a period of 24 h at 37 °C. Then, sterile phosphate buffer (220 lL) was used to wash the contents of each well three times. Each of the plates was given a vigorous shaking in order to get rid of any nonadherent bacteria. The remaining attached bacteria were fixed by using 220 μL of 99% methanol in each well; after 15 min, each plate was emptied and dried. Then, 220 mL of 50% crystal violet was added to each well for 5 min in order to stain all of the wells, while running tap water was used to remove the excess stain from each plate. Finally, the plates were dried in air, while 220 mL of 33% (v/v) glacial acetic acid was added to each well for resolubilization of the dye bound to adherent cells. A microplate reader (BioTek) was used to measure the OD of each well at 630 nm.[37] Every experiment was revised three times against each bacterium, and the final results were considered by noting the average of all three measured values. The following formula was applied to determine the bacterial growth inhibition (INH%):

$$\mathrm{INH\%} = 100 - (\mathrm{OD_{630sample}}^{*}100)/\mathrm{OD_{630control}} \quad (3)$$

Determination of the Antibacterial Activity by the Agar Well Diffusion Method. The agar well diffusion method was used to test the antibacterial potential[38] of the synthesized NPs using ciprofloxacin as the reference drug. To a freshly prepared suspension of nutrient agar (37 g L^{-1}) in distilled water, 0.1 N HCl/NaOH was added to adjust its pH to 7. This growth medium was sterilized for 15 min in an autoclave at 121 °C and then poured into sterilized Petri plates. Subsequently, 100 μL of the inoculum of a test bacterium (*S. aureus* and *E. coli*) was added and mixed homogeneously with the growth medium in the Petri plate. Then, the mixture was solidified, followed by cutting wells of fixed diameters by a sterilized borer in the solidified agar. Afterward, 50 μL of the test/reference sample was poured into each well under aseptic conditions in a laminar air-flow cabinet. After incubation of the Petri plates for 24 h at 37 °C, inhibition zones were formed around the wells, whose diameters were measured in millimeters using a vernier caliper. The observed diameters of inhibition zones were compared with those of ciprofloxacin.[38]

CONCLUSIONS

Green synthesis of nanoparticles is an emerging field of research today and has evolved as an environmentally safe, cost-effective, and nontoxic approach. *T. erecta* leaf and petal extracts were successfully used to produce $(Mn_3O_4)_L$ and

https://doi.org/10.1021/acsomega.4c01328
ACS Omega 2024, 9, 35408−35419

$(Mn_3O_4)_P$ NPs, respectively. The FTIR spectra showed Mn−O stretching modes in tetragonal sites, characterized by sharp peaks at 605.69 and 616.87 cm^{-1} in $(Mn_3O_4)_L$ and $(Mn_3O_4)_P$, respectively. Raman spectroscopy revealed the existence of tetrahedral and octahedral units along with A_{1g}, T_{2g}, and E_g active modes of Mn_3O_4 and 2TO mode. UV−visible analyses of $(Mn_3O_4)_L$ and $(Mn_3O_4)_P$ NPs showed absorption peaks at 272.3 and 268.8 nm along with band gaps of 4.83 and 5.49 eV, respectively. The production of Mn_3O_4 in a tetragonal body-centered lattice structure was confirmed by the results extracted from the XRD investigation. The average crystallite size (19.24 nm) of $(Mn_3O_4)_P$ was smaller than that (20.84 nm) of $(Mn_3O_4)_L$ NPs. SEM images displayed the porous and spherical morphologies of NPs, with a diameter of 15−35 nm. TGA curves demonstrated good thermal stabilities, the hydrous nature of NPs, and the loss of moisture with an increase in temperature. The DSC curves of $(Mn_3O_4)_P$ and $(Mn_3O_4)_L$ exhibited endothermic peaks at 189.6 and 201.9 °C and exothermic peaks at 333.2 and 513.1 °C, respectively, with glass transition temperatures of 258.9 and 308.7 °C, respectively. CV curves of Mn_3O_4 NPs clearly indicated redox peaks and led to redox reactions. GCD scans illustrated the capacitive behavior of the synthesized nanoparticles and their suitability for capacitor electrodes. The synthesized NPs were also tested for their antibacterial efficacy by biofilm inhibition and agar well diffusion procedures. The NPs showed higher activities against *S. aureus* (Gram-positive) than against *E. coli* (Gram-negative). Moreover, $(Mn_3O_4)_P$ was more active than (Mn_3O_4) due to differences in the phytochemical nature of their surface coatings. The investigated biosynthetic route is eco-friendly because it involves *T. erecta* leaves and petals as the reductant as well as the coating agent, in spite of involving toxic chemical compounds.

AUTHOR INFORMATION

Corresponding Authors

Shabbir Hussain − *Institute of Chemistry, Khwaja Fareed University of Engineering and Information Technology, Rahim Yar Khan 64200, Pakistan;* orcid.org/0000-0002-6979-5687; Email: shabchem786@gamil.com

Fezah Othman − *Department of Biomedical Sciences, Faculty of Medicine and Health Sciences, Universiti Putra Malaysia, Serdang 43400 Selangor, Malaysia*; Email: fezah@upm.edu.my

Zainul Amiruddin Zakaria − *Borneo Research on Algesia, Inflammation and Neurodegeneration (BRAIN) Group, Department of Biomedical Sciences, Faculty of Medicine and Health Sciences, Universiti Malaysia Sabah, Kota Kinabalu 88400 Sabah, Malaysia; Department of Environmental Health, Faculty of Public Health, Campus C Universitas Airlangga, Jalan Mulyorejo Surabaya 60115 East Java, Indonesia*; Email: zaz@ums.edu.my

Authors

Ammara Aslam − *Department of Chemistry, Lahore Garrison University, Lahore 54792, Pakistan*

Affifa Tajammal − *Department of Chemistry, Lahore Garrison University, Lahore 54792, Pakistan*

Zeeshan Mustafa − *Department of Physics, Lahore Garrison University, Lahore 54792, Pakistan*

Amnah Mohammed Alsuhaibani − *Department of Physical Sport Science, College of Sport Sciences & Physical Activity, Princess Nourah bint Abdulrahman University, Riyadh 11671, Saudi Arabia*

Moamen Salaheldeen Refat − *Department of Chemistry, College of Science, Taif University, Taif 21944, Saudi Arabia*

Muhammad Shahid − *Department of Chemistry and Biochemistry, University of Agriculture, Faisalabad 38000, Pakistan*

Muhammad Sagir − *Institute of Chemical and Environmental Engineering, Khwaja Fareed University of Engineering and Information Technology, Rahim Yar Khan 64200, Pakistan*

Complete contact information is available at: https://pubs.acs.org/10.1021/acsomega.4c01328

Notes

The authors declare no competing financial interest.

ACKNOWLEDGMENTS

The authors acknowledge the Princess Nourah bint Abdulrahman University Researchers Supporting Project number (PNURSP2024R65), Princess Nourah bint Abdulrahman University, Riyadh, Saudi Arabia.

REFERENCES

(1) Fang, X.; Cheng, X.; Zhang, Y.; Zhang, L. G.; Keidar, M. Single-step synthesis of carbon encapsulated magnetic nanoparticles in arc plasma and potential biomedical applications. *J. Colloid Interface Sci.* **2018**, *509*, 414−421.

(2) Munir, M.; Hussain, S.; Anwar, R.; Waqas, M.; Ali, J. The Role of Nanoparticles in the Diagnosis and Treatment of Diseases. *Sci. Inquiry Rev.* **2021**, *4* (3), 14−26.

(3) Shahzad, K.; Karim, I.; Abbass, S. M.; Karim, H. K. H.; Hussain, S.; Ashfaq, M.; Rehman, M. Synthesis, Characterization, and Photocatalytic Degradation of Nickel Doped Copper Oxide Nanoparticles. *Lahore Garrison Univ. J. Life Sci.* **2021**, *4* (02), 130−138.

(4) Javed, M.; Abid, M. A.; Hussain, S.; Shahwar, D.; Arshad, S.; Ahmad, N.; Arif, M.; Khan, H.; Nadeem, S.; Raza, H.; Harron, S. M. Synthesis, characterization and photocatalytic applications of s-doped graphitic carbon nitride nanocomposites with nickel doped zinc oxide nanoparticles. *Dig. J. Nanomater. Biostruct.* **2020**, *15*, 1097−1105, DOI: 10.15251/DJNB.2020.154.1097.

(5) Iqbal, M.; Muneer, M.; Raza, R.; Saleem, M.; Hussain, S.; Rehman, Z. U.; Abbas, F.; Ali, S.; Javed, M. A.; Hussain, M. Recycling of lead from lead acid battery to form composite material as an anode for low temperature solid oxide fuel cell. *Mater. Today Energy* **2020**, *16*, No. 100418.

(6) Kharangarh, P. R.; Ravindra, N. M.; Singh, G.; Umapathy, S. Synthesis and characterization of Nb-doped strontium cobaltite@GQD electrodes for high performance supercapacitors. *J. Energy Storage* **2022**, *55*, No. 105388.

(7) Javed, M.; Abbas, S. M.; Hussain, S.; Siddiq, M.; Han, D.; Niu, L. Amino-functionalized silica anchored to multiwall carbon nanotubes as hybrid electrode material for supercapacitors. *Mater. Sci. Energy Technol.* **2018**, *1* (1), 70−76.

(8) Khan, N. A.; Imran, M.; Akhtar, M. N.; Hussain, S.; Khan, M. A.; Shami, A.; Iqbal, H. Remediation of organic pollutant from the aqueous environment using in-house fabricated polyaniline-based hybrid composite (PANI-MnPBA/NiCoMnS) materials. *Chemosphere* **2024**, *350*, No. 141077.

(9) Rehman, H.; Ali, Z.; Hussain, M.; Gilani, S. R.; Shahzady, T. G.; Zahra, A.; Hussain, S.; Hussain, H.; Hussain, I.; Farooq, M. U. Synthesis and characterization of ZnO nanoparticles and their use as an adsorbent for the arsenic removal from drinking water. *Dig. J. Nanomater. Biostruct.* **2019**, *14* (4), 1033−1040.

(10) Prasad, V.; Lukose, S.; Prasad, L. Emerging forensic applications of nanotechnology. *Int. J. Eng. Allied Sci.* **2016**, *2*, 1−8.

https://doi.org/10.1021/acsomega.4c01328
ACS Omega 2024, 9, 35408−35419

(11) Liu, X.; Chen, C.; Zhao, Y.; Jia, B. A review on the synthesis of manganese oxide nanomaterials and their applications on lithium-ion batteries. *J. Nanomater.* **2013**, *2013*, No. 736375, DOI: 10.1155/2013/736375.
(12) Sackey, J.; Akbari, M.; Morad, R.; Bashir, A.; Ndiaye, N.; Matinise, N.; Maaza, M. Molecular dynamics and bio-synthesis of phoenix dactylifera mediated Mn3O4 nanoparticles: Electrochemical application. *J. Alloys Compd.* **2021**, *854*, No. 156987.
(13) Vu, C. M.; Ghotekar, S.; Viet, N. M.; Dabhane, H.; Oza, R.; Roy, A. Green Synthesis of Plant-assisted Manganese-based Nanoparticles and their Various Applications. In *Plant and Nanoparticles*; Springer, 2022; pp 339−354.
(14) Prajapati, J. P.; Singh, P.; Singh, K. R.; Singh, J.; Mallick, S.; Singh, R. P. Biogenic synthesis of Mn3O4 NPs using Phyllanthus emblica leaf extract for electrochemical sensing of urea. *J. Mol. Struct.* **2024**, *1307*, No. 137918, DOI: 10.1016/j.molstruc.2024.137918.
(15) Ahmad, K. S.; Yaqoob, S.; Gul, M. M. Dynamic green synthesis of iron oxide and manganese oxide nanoparticles and their cogent antimicrobial, environmental and electrical applications. *Rev. Inorg. Chem.* **2022**, *42* (3), 239−263.
(16) Abuzeid, H. M.; Julien, C. M.; Zhu, L.; Hashem, A. M. Green Synthesis of Metal and Metal Oxide Nanoparticles for Recent Applications. *Crystals* **2023**, *13*, No. 1576, DOI: 10.3390/cryst13111576.
(17) Yasmeen, G.; Hussain, S.; Tajammal, A.; Mustafa, Z.; Sagir, M.; Shahid, M.; Ibrar, M.; Elqahtani, Z. M.; Iqbal, M.; et al. Green Synthesis of Cr2O3 Nanoparticles by Cassia Fistula, their Electrochemical and Antibacterial Potential. *Arabian J. Chem.* **2023**, *16*, No. 104912, DOI: 10.1016/j.arabjc.2023.104912.
(18) Kaur, K.; Sidhu, A. K. Green synthesis: An eco-friendly route for the synthesis of iron oxide nanoparticles. *Front. Nanotechnol.* **2021**, *3*, 47.
(19) Diallo, A.; Tandjigora, N.; Ndiaye, S.; Jan, T.; Ahmad, I.; Maaza, M. Green synthesis of single phase hausmannite Mn3O4 nanoparticles via Aspalathus linearis natural extract. *SN Appl. Sci.* **2021**, *3*, 1−11.
(20) Pandey, V.; Adiba, A.; Munjal, S.; Ahmad, T. Structural and magnetic properties of tetragonal Mn3O4 nanoparticles synthesized by sol-gel method. *AIP Conf. Proc.* **2020**, *2220*, No. 020163, DOI: 10.1063/5.0001796.
(21) Chouchaine, A.; Marzouk-Trifi, I.; Trifi, B.; Ghodbane, O.; Dhaouadi, H.; Touati, F.; Amdouni, N.; Kouass, S. Synthesis, characterization of Mn3O4: adsorption application and antibacterial evaluation. *J. Chil. Chem. Soc.* **2022**, *67* (3), 5582−5586.
(22) Mylarappa, M.; Lakshmi, V. V.; Mahesh, K. V.; Nagaswarupa, H.; Raghavendra, N. A facile hydrothermal recovery of nano sealed MnO2 particle from waste batteries: An advanced material for electrochemical and environmental applications. *IOP Conf. Ser.: Mater. Sci. Eng.* **2016**, *149*, No. 012178, DOI: 10.1088/1757-899X/149/1/012178.
(23) Vázquez-Olmos, A.; Redón, R.; Rodríguez-Gattorno, G.; Mata-Zamora, M. E.; Morales-Leal, F.; Fernández-Osorio, A. L.; Saniger, J. M. One-step synthesis of Mn3O4 nanoparticles: Structural and magnetic study. *J. Colloid Interface Sci.* **2005**, *291* (1), 175−180.
(24) Mironova-Ulmane, N.; Kuzmin, A.; Skvortsova, V. N.; Chikvaidze, G.; Sildos, I.; Grabis, J.; Jankovica, D.; Dindune, A. P.; Maiorov, M. M. Synthesis and vibration spectroscopy of nano-sized manganese oxides. *Acta Phys. Pol., A* **2018**, *133* (4), 1013−1016.
(25) Ma, H.; Wu, C. Feasibility and Performance Evaluation of Cementitious Material Mixed with Coal Gangue Solid Waste. In *Managing Mining and Minerals Processing Wastes*; Elsevier, 2023; pp 99−130.
(26) Mojet, B. L.; Ebbesen, S. D.; Lefferts, L. Light at the interface: the potential of attenuated total reflection infrared spectroscopy for understanding heterogeneous catalysis in water. *Chem. Soc. Rev.* **2010**, *39* (12), 4643−4655.
(27) Amer, A. A.; Reda, S.; Mousa, M.; Mohamed, M. M. Mn3O4/graphene nanocomposites: outstanding performances as highly efficient photocatalysts and microwave absorbers. *RSC Adv.* **2017**, *7* (2), 826−839.
(28) Sharma, J. K.; Srivastava, P.; Ameen, S.; Akhtar, M. S.; Singh, G.; Yadava, S. Azadirachta indica plant-assisted green synthesis of Mn3O4 nanoparticles: Excellent thermal catalytic performance and chemical sensing behavior. *J. Colloid Interface Sci.* **2016**, *472*, 220−228.
(29) Julien, C. M.; Massot, M. Raman spectroscopic studies of lithium manganates with spinel structure. *J. Phys.: Condens. Matter* **2003**, *15* (19), No. 3151, DOI: 10.1088/0953-8984/15/19/315.
(30) Julien, C.; Massot, M.; Baddour-Hadjean, R.; Franger, S.; Bach, S.; Pereira-Ramos, J. Raman spectra of birnessite manganese dioxides. *Solid State Ionics* **2003**, *159* (3−4), 345−356.
(31) Tian, Z.-Y.; Mountapmbeme Kouotou, P.; Bahlawane, N.; Tchoua Ngamou, P. H. Synthesis of the catalytically active Mn3O4 spinel and its thermal properties. *J. Phys. Chem. C* **2013**, *117* (12), 6218−6224.
(32) Kim, M.; Chen, X.; Joe, Y. I.; Fradkin, E.; Abbamonte, P.; Cooper, S. L. Mapping the magnetostructural quantum phases of Mn3O4. *Phys. Rev. Lett.* **2010**, *104* (13), No. 136402.
(33) Gao, T.; Glerup, M.; Krumeich, F.; Nesper, R.; Fjellvåg, H.; Norby, P. Microstructures and spectroscopic properties of cryptomelane-type manganese dioxide nanofibers. *J. Phys. Chem. C* **2008**, *112* (34), 13134−13140.
(34) Dubal, D.; Dhawale, D.; Salunkhe, R.; Fulari, V.; Lokhande, C. Chemical synthesis and characterization of Mn3O4 thin films for supercapacitor application. *J. Alloys Compd.* **2010**, *497* (1−2), 166−170.
(35) Gosens, I.; Post, J. A.; de la Fonteyne, L. J.; Jansen, E. H.; Geus, J. W.; Cassee, F. R.; de Jong, W. H. Impact of agglomeration state of nano-and submicron sized gold particles on pulmonary inflammation. *Part. Fibre Toxicol.* **2010**, *7* (1), 1−11.
(36) Ding, B.; Zheng, P.; Ma, P.; Lin, J. Manganese oxide nanomaterials: synthesis, properties, and theranostic applications. *Adv. Mater.* **2020**, *32* (10), No. 1905823.
(37) Anjum, F.; Bukhari, S. A.; Shahid, M.; Bokhari, T. H.; Talpur, M. M. A. Exploration of nutraceutical potential of herbal oil formulated from parasitic plant. *Afr. J. Tradit., Complementary Altern. Med.* **2014**, *11* (1), 78−86.
(38) Mushtaq, Z.; Khan, U.; Seher, N.; Shahid, M.; Shahzad, M.; Bhatti, A.; Sikander, T. Evaluation of antimicrobial, antioxidant and enzyme inhibition roles of polar and non-polar extracts of clitoria ternatea seeds. *J. Anim. Plant Sci.* **2021**, *31* (5), 1405−1418, DOI: 10.36899/JAPS.2021.5.0342.
(39) Beveridge, T. J. Structures of gram-negative cell walls and their derived membrane vesicles. *J. Bacteriol.* **1999**, *181* (16), 4725−4733.
(40) Fivenson, E. M.; Rohs, P. D.; Vettiger, A.; Sardis, M. F.; Torres, G.; Forchoh, A.; Bernhardt, T. G. A role for the Gram-negative outer membrane in bacterial shape determination. *Proc. Natl. Acad. Sci. U.S.A.* **2023**, *120* (35), No. e2301987120.
(41) Rohde, M. The Gram-positive bacterial cell wall. *Microbiol. Spectrum* **2019**, *7* (3), 10−1128, DOI: 10.1128/microbiolspec.GPP3-0044-2018.
(42) Padalia, H.; Chanda, S. Antimicrobial efficacy of different solvent extracts of Tagetes erecta L. flower, alone and in combination with antibiotics. *Appl. Microbiol.: Open Access* **2015**, *1* (1), 1−10.
(43) Binjawhar, D. N.; Al-Enazi, N. M.; Alsamhary, K.; Kha, M. Plant mediated biosynthesis of Mn3O4 nanostructures and their biomedical applications. *Heliyon* **2024**, *10*, No. 27695, DOI: 10.1016/j.heliyon.2024.e27695.
(44) Ramesh, R.; Catherine, G.; Sundaram, S. J.; Khan, F. L. A.; Kaviyarasu, K. Synthesis of Mn3O4 nano complex using aqueous extract of Helianthus annuus seed cake and its effect on biological growth of Vigna radiata. *Mater. Today: Proc.* **2021**, *36*, 184−191.
(45) Nair Sreekala, G.; Abdullakutty, F.; Beena, B. Green synthesis, characterization, and photo catalytic degradation efficiency of Trimanganese Tetroxide nanoparticle. *Int. J. Nano Dimens.* **2019**, *10* (4), 400−409.

(46) Ibrahim, A.; Hammadi, M. Green Synthesis of Mn3O4 Nanoparticles using chia seeds extract, characterization, and cytotoxicity on the HL-60 cells. *Hist. Med.* **2023**, *9* (1), 1537−1542.
(47) Adeyemi, J. O.; Onwudiwe, D. C.; Oyedeji, A. O. In vitro α-glucosidase enzyme inhibition and anti-inflammatory studies of Mn3O4 nanoparticles mediated using extract of dalbergiella welwitschia. *Results Chem.* **2022**, *4*, No. 100497.
(48) Aarthi, R.; Anitha, P. Biological synthesis of manganese oxide nanoparticles from aerial parts of Prunus dulcis and their in vitro investigation of medical properties. *Appl. Organomet. Chem.* **2023**, *37* (12), No. e7283.
(49) Salmi, C.; Souhaila, M.; Salah Eddine, L.; Mohammed, H. A. M.; Hasan, G. G.; Mahboub, M. S. Biosynthesis of Mn3O4/PVP nanocomposite for enhanced photocatalytic degradation of organic dyes under sunlight irradiation. *J. Cluster Sci.* **2024**, *35*, 201−215.
(50) Liu, M.; Lin, M.; Wu, P.; Owens, G.; Chen, Z. A new catalyst for the activation of peroxydisulfate: Carbonized manganese oxides nanoparticles derived from green tea extracts. *Sep. Purif. Technol.* **2023**, *310*, No. 123052.
(51) Tran, T. V.; Nguyen, D. T. C.; Kumar, P. S.; Din, A. T. M.; Qazaq, A. S.; Vo, D.-V. N. Green synthesis of Mn3O4 nanoparticles using Costus woodsonii flowers extract for effective removal of malachite green dye. *Environ. Res.* **2022**, *214*, No. 113925.
(52) Wyantuti, S.; Hartati, Y. W.; Panatarani, C.; Tjokronegoro, R. Cyclic voltammetric study of Chromium (VI) and Chromium (III) on the gold nanoparticles-modified glassy carbon electrode. *Procedia Chem.* **2015**, *17*, 170−176.

https://doi.org/10.1021/acsomega.4c01328
ACS Omega 2024, 9, 35408−35419